

3D development of detachment faulting during continental breakup

Lymer, Gaël; Cresswell, Derren; Reston, Timothy; Bull, JM; Sawyer, DS; Morgan, JK; Stevenson, Carl; Causer, Annabel; Minshull, Tim; Shillington, DJ

DOI:

[10.1016/j.epsl.2019.03.018](https://doi.org/10.1016/j.epsl.2019.03.018)

License:

Creative Commons: Attribution-NonCommercial-NoDerivs (CC BY-NC-ND)

Document Version

Peer reviewed version

Citation for published version (Harvard):

Lymer, G, Cresswell, D, Reston, T, Bull, JM, Sawyer, DS, Morgan, JK, Stevenson, C, Causer, A, Minshull, T & Shillington, DJ 2019, '3D development of detachment faulting during continental breakup', *Earth and Planetary Science Letters*, vol. 515, pp. 90-99. <https://doi.org/10.1016/j.epsl.2019.03.018>

[Link to publication on Research at Birmingham portal](#)

Publisher Rights Statement:

Checked for eligibility: 09/04/2019

General rights

Unless a licence is specified above, all rights (including copyright and moral rights) in this document are retained by the authors and/or the copyright holders. The express permission of the copyright holder must be obtained for any use of this material other than for purposes permitted by law.

- Users may freely distribute the URL that is used to identify this publication.
- Users may download and/or print one copy of the publication from the University of Birmingham research portal for the purpose of private study or non-commercial research.
- User may use extracts from the document in line with the concept of 'fair dealing' under the Copyright, Designs and Patents Act 1988 (?)
- Users may not further distribute the material nor use it for the purposes of commercial gain.

Where a licence is displayed above, please note the terms and conditions of the licence govern your use of this document.

When citing, please reference the published version.

Take down policy

While the University of Birmingham exercises care and attention in making items available there are rare occasions when an item has been uploaded in error or has been deemed to be commercially or otherwise sensitive.

If you believe that this is the case for this document, please contact UBIRA@lists.bham.ac.uk providing details and we will remove access to the work immediately and investigate.

1 **3D development of detachment faulting during continental breakup**

2

3 **Gaël Lymer^{1*}, Derren J F Cresswell¹, Tim J Reston¹, Jonathan M Bull², Dale S Sawyer³,**
4 **Julia K Morgan³, Carl Stevenson¹, Annabel Causer¹, Tim A Minshull², Donna J**
5 **Shillington⁴;**

6

7 **¹School of Geography, Earth and Environmental Science, University Birmingham, UK**

8 **²School of Ocean and Earth Sciences, University of Southampton, UK**

9 **³Department of Earth Science, Rice University, Houston, Texas**

10 **⁴Lamont-Doherty Earth Observatory, Palisades, New York, USA.**

11 ***Corresponding author: G. Lymer**

12 **ABSTRACT**

13 The developing asymmetry of rifting and continental breakup to form rifted margins has been
14 much debated, as has the formation, mechanics and role of extensional detachments. Bespoke
15 3D seismic reflection data across the Galicia margin, west of Spain, image in unprecedented
16 detail an asymmetric detachment (the S reflector). Mapping S in 3D reveals its surface is
17 corrugated, proving that the overlying crustal blocks slipped on S surface during the rifting.
18 Crucially, the 3D data show that the corrugations on S perfectly match the corrugations
19 observed on the present-day block-bounding faults, demonstrating that S is a composite
20 surface, comprising the juxtaposed rotated roots of block-bounding faults as in a rolling hinge
21 system with each new fault propagation moving rifting oceanward; changes in the orientation
22 of the corrugations record the same oceanward migration. However, in contrast to previous
23 rolling hinge models, the slip of the crustal blocks on S occurred at angles as low as $\sim 20^\circ$,
24 requiring that S was unusually weak, consistent with the hydration of the underlying mantle

25 by seawater ingress following the embrittlement of the entire crust. As the crust only becomes
26 entirely brittle once thinned to ~10 km, the asymmetric S detachment and the hyper-extension
27 of the continental crust only developed late in the rifting process, which is consistent with the
28 observed development of asymmetry between conjugate magma poor margin pairs. The 3D
29 volume allows analysis of the heaves and along strike architecture of the normal faults, whose
30 planes laterally die or spatially link together, implying overlaps in faults activity during
31 hyper-extension. Our results thus reveal for the first time the 3D mechanics and timing of
32 detachment faulting growth, the relationship between the detachment and the network of
33 block-bounding faults above it and the key processes controlling the asymmetrical
34 development of conjugate rifted margins.

35 **KEY WORDS**

36 **Rifting processes; Galicia margin; North Atlantic Ocean; Detachment fault; Assymetry;**
37 **3D seismic reflection**

38

39 **1 INTRODUCTION**

40 The rifting and breakup of the continents to form new ocean basins (Bullard et al, 1965; Le
41 Pichon and Sibuet, 1981; Lister et al., 1986) is a first order tectonic process at the surface of
42 the Earth that changes ocean circulation by opening new oceanographic gateways (Barker and
43 Burrell, 1977; Reston, 2010), leads to evolutionary divergence through biotic diaspora (Fortey
44 and Cocks, 2003) and creates the environment for the accumulation of thick piles of
45 sediments that host important resources (e.g. Lentini et al., 2010). Yet the processes of
46 hyperextension and asymmetrical development of conjugate margins leading to eventual
47 continental breakup remain poorly understood (Reston et al., 2007; Ranero and Pérez-
48 Gussinyé, 2010; Brune et al. 2014).

49 Much recent debate has centred on the importance of sequential faulting (Goldsworthy and
50 Jackson, 2001; Ranero and Pérez-Gussinyé, 2010; Brune et al., 2014), in which extension
51 occurs along a succession of individual faults, which develop, rotate and lock *before* the
52 succeeding fault initiates by slicing ever farther into one side of the rift, thus creating the
53 asymmetry of the resulting conjugate margins (Ranero and Pérez-Gussinyé, 2010). Sequential
54 faulting and the resulting asymmetry has been proposed to develop early in the rifting process
55 when the continental crust is still >20 km thick (Ranero and Pérez-Gussinyé, 2010), but
56 dynamic models (Brune et al., 2014) allow a later onset, more consistent with observations
57 from North Atlantic magma-poor conjugate margins (Reston, 2010), which show that the
58 asymmetry only developed when the crust had thinned to <10 km to become entirely brittle
59 (Reston and Pérez-Gussinyé, 2007; Reston, 2010). Related questions concern the
60 development and mechanics of apparently low-angle, large-displacement “detachment” faults
61 (Lister et al., 1986; Hoffmann and Reston, 1992; Sibuet, 1992): how and when these
62 detachments formed and whether they slipped at low-angles (Figure 1a) or developed by a
63 rolling hinge mechanism (Buck, 1988; Figure 1b). The rolling hinge model itself is a form of
64 sequential faulting in which the “detachment” comprises segments of successive steep faults
65 (Buck, 1988; Reston et al., 2007; Choi et al., 2013), each active individually and in turn, each
66 abandoned when a new fault cuts through the hanging wall of the previous fault, and each
67 rotated by slip on subsequent faults propagating up from a steep root zone to form an
68 apparently continuous sub-horizontal surface (Figure 1b).

69

70 Many of the key concepts of rifting processes have been developed and/or tested at the
71 Galicia margin, west of Spain, where the now widely observed characteristics (Reston, 2010)
72 of reduced mantle velocities beneath thin crust, the crust thinning toward zero, and mantle
73 unroofing (Boillot and Winterer, 1988), were first recognised. This margin is both sediment-

74 starved and magma-poor (Boillot and Winterer, 1988), allowing an optimal image of the
75 margin structure, including well-defined extensional faults (Reston et al., 2007; Ranero and
76 Pérez-Gussinyé, 2010) which appear to detach onto a band of bright discontinuous reflections
77 termed collectively the S reflector (de Charpal et al., 1978; Boillot and Winterer, 1988), and
78 identified as a possible detachment fault (Sibuet, 1992; Reston et al., 2007). The final root of
79 S is believed to be currently located on the conjugate Flemish Cap margin (Reston et al.,
80 2007; Ranero and Pérez-Gussinyé, 2010), where it forms a bright reflection dipping
81 landwards at 30° (Hopper et al., 2004).

82

83 Studies of continental rifts (Cowie et al., 2005; Nixon et al., 2016) and of seafloor spreading
84 (Cann et al., 1997) have shown that the process of continental rifting and eventual breakup is
85 complex and three-dimensional (3D). However, current understanding of the Galicia margin
86 and of continental breakup in general has been based on 2D numerical models (Huisman and
87 Beaumont, 2003; Brune et al., 2014), 2D datasets particularly seismic reflection profiles (e.g.
88 de Charpal et al., 1978; Reston et al., 2007; Ranero and Pérez-Gussinyé, 2010), drilling
89 transects (Boillot and Winterer, 1988; Whitmarsh et al., 1998) and industry data not designed
90 or located to address the key scientific questions. In this paper, we present results from the
91 interpretation of a 3D seismic volume located offshore Spain (Figure 2), designed specifically
92 to reveal for the first time the 3D structures generated during the rifting of the Galicia margin.
93 The 3D data uncover the timing and mechanics of faulting and of asymmetric detachment
94 development, and show that both are compatible with the inferred onset of asymmetry at other
95 magma-poor margins (Reston, 2010), thus providing important new insights into the
96 mechanisms of continental breakup at magma-poor margins worldwide.

97

98 **2 THE GALICIA 3D VOLUME**

99 The seismic data were collected in 2013 (Figure 2) with the RV Marcus Langseth, towing two
100 3300 cu in tuned airgun arrays, firing alternately every 37.5 m. The data were received by
101 four digital hydrophone streamers, each 6 km in length, containing 480 channels and towed
102 with a 200 m spacing, producing a 68.5km x 20 km volume down to 14s TWT with a nominal
103 inline spacing of 6.25 m and a cross-line spacing of 50m. Processing was carried out by
104 Repsol and consisted of editing, despiking and low cut filtering, wavelet shaping including
105 zero phase conversion, multiple suppression (surface related multiple elimination and radon
106 demultiple), static correction to correct for variation in water velocity during the experiment,
107 offset plane Fourier regularisation and binning to 12.5 m inline and 25 m crossline spacing,
108 3D prestack time migration after tomographic and residual moveout velocity analysis, and
109 bandpass filtering. Relative amplitudes were preserved in the data shown here, although an
110 amplitude balanced version was also used for interpretation. The time migrated image was
111 converted to depth using a velocity model constructed from the interpretation of the fault
112 block structure, using velocities from wide-angle data and from 2D prestack depth migrations:
113 the depth image was compared with coincident images produced by 2D prestack depth
114 migration to ratify the depth conversion (Supplementary Figure S1). Interpretation was via the
115 Kingdom suite: uninterpreted versions of the seismic sections presented are shown in
116 Supplementary Figure S2.

117

118 **3 MARGIN STRUCTURE**

119 The 3D volume (Figure 3) provides spectacular new images and observations of the 3D
120 structure of the Galicia margin, including sedimentary layering tilted, folded and faulted
121 within the fault blocks by complex intrablock faulting, the architecture of the block-bounding
122 faults network, whose deepest juxtaposed segments successively form the oceanward

123 continuity of the S reflector, confirming that S is some form of detachment fault. We number
124 the faults F3 through F6 following the 2D classification of Ranero and Pérez-Gussinyé
125 (2010), but as the faults splay and die out laterally in 3D, we have added suffixes, thus
126 keeping the same basic numbering scheme but distinguishing between the many faults. The
127 block-bounding faults also bound wedges of sediment that splay towards the faults which we
128 identify as synrift and discuss further below.

129 **3.1 The 3D geometry of the S detachment**

130 In the volume, S is a strong, simple, apparently continuous reflection at ~ 9s TWT marking
131 the base of a probable damage zone (Leythaeuser et al., 2005; Schuba et al., 2018) at the main
132 fault interface. Mapped in time (Figure 4a), S shows long-wavelength undulations that are due
133 to velocity pull-up effects of the overlying fault blocks. S also shows pronounced
134 corrugations that are oblique to the sail-lines and thus are not acquisition artefacts. The
135 corrugations correspond to ~ 10 ms lineations in a filtered map of S (Figure 4b), persist after
136 depth conversion (Figure 4c) and match high-amplitude lineations on the amplitude map of S
137 (Figure 4d). Corrugations observed on major slip surfaces, such as on oceanic detachment
138 faults (Cann et al., 1997), are believed to form at depth and to parallel the displacement
139 direction (Resor and Meer, 2009; Edwards et al., 2018), but have never previously been
140 observed on a major extensional detachment buried beneath fault blocks at a rifted margin
141 before the acquisition of the Galicia 3D volume. In both time and depth, the corrugations
142 exhibit an oceanward change in orientation from E-W to ESE-WNW; the identification and
143 changing orientation of the corrugations on S demonstrate that the overlying extended
144 continental crust slipped on S and that the direction of extension changed oceanwards,
145 remaining parallel to the corrugations (Figure 4), during the rifting. The dominant strike of
146 the faults also changes oceanwards from N-S to SSW-NNE, remaining approximately

147 perpendicular to the corrugations and suggesting that the corrugations formed at the same
148 time as the faults overlying them.

149 A spectacular observation from the Galicia 3D volume is that the corrugations of the S
150 surface align with corrugations observed on some of the block-bounding fault planes (Figure
151 3, F6.0): many of the block-bounding fault surfaces were subject to mass-wasting when
152 exposed at the seafloor, obscuring any corrugations that may have formed, but some fault
153 planes, such as F6.0, display preserved corrugations (Figure 3) where they juxtapose
154 hangingwall and footwall basement (and so were never subject to mass-wasting); corrugations
155 on fault F6.0 (Figure 3) do not just align with the corrugations on S, but accurately match
156 ridge and trough with the corrugations on S, suggesting that both fault F6.0 and S represented
157 a single slip surface when F6.0 was active and the corrugations formed. The close relationship
158 between the activity of one fault and the development of S, emphasized by the matching of
159 the corrugations on both surfaces, strongly supports the development of S following a rolling
160 hinge model in which the basal detachment is composed of root segments of block-bounding
161 faults. Another characteristic of the rolling-hinge model (Buck, 1988; Choi et al., 2013) is
162 the upward propagation of the faults from a deep root zone, and we interpret the continuity of
163 corrugations on S and overlying faults (Figure 3) as evidence that both surfaces have
164 slipped together, suggesting that the block-bounding faults propagated up from S, consistent
165 with the rolling-hinge model. Nucleation of the faults on S and upward propagation
166 are further supported by the upward decrease in fault displacements (Figure 5) and the
167 increase in geometric complexity of the fault network between the S and the top basement
168 surfaces (Figures 4 and 6) that we interpret as resulting from the splitting of fault branches as
169 they propagated up in the shallower units.

170

171 Depth conversion removes the pull-up effects of the overlying fault blocks (Figure 4c) but
172 pronounced topography on S remains where S meets the crust-mantle boundary (green-dotted
173 line on Figure 4) and where the deep segments of some of the block-bounding faults form the
174 oceanward propagation of S (solid coloured lines on Figure 4). Fault-related distortions of S
175 are also apparent on the time sections (Figure 5; Schuba et al., 2018), on the time structure
176 map (Figure 4a), and on the depth map of S, especially after removing the long-wavelength
177 topography related to velocity pull-up effects (Figure 4c), and thus are not products of the
178 depth conversion but genuine features of S. Uninterpreted maps showing fault-related
179 distortions on the S surface both in time and depth are presented in Supplementary Figure S3.

180

181 The continuity of the corrugations between faults and S (Figure 3), and the topographic
182 distortions on S where the faults root on it (Figures 4 and 5) both emphasize the partitioned
183 nature of S, i.e. that S comprises the downdip portions of successive fault planes, consistent
184 with the rolling hinge model (Buck, 1988; Reston et al., 2007; Choi et al., 2013). In the 2D
185 rolling hinge model (Buck, 1988; Choi et al., 2013), extension over any one-time interval is
186 along a single fault, rooting steeply at depth, that flexurally rotates as the crust beneath the
187 fault is gradually pulled out from beneath the hangingwall. When rotated sufficiently, the
188 fault is abandoned and replaced by a single new fault that initiates after the previous fault is
189 locked (Buck, 1988; Choi et al., 2013) cutting up from the same root zone and across the
190 preceding fault, now part of S, at a slight angle to transfer a slice of the hangingwall to the
191 footwall. However, only some of the block-bounding faults (e.g., faults 3.1; 5.1; 5.4; 6.1; 6.4
192 on Figure 5) appear to distort and cut across the more landward portions of S, but others just
193 merge with or stop abruptly at S. We suggest that those faults which cut at a low-angle across
194 the more landward portion of S bound groups or families of faults active over the same time,
195 as supported by fault heave analysis (see next section).

196 **3.2 3D relationships between faults**

197 To investigate the relationship between faults in 3D and to identify which faults must have
198 been active over the same time, we mapped the spatial relationships between the fault planes
199 of the main block-bounding faults and measured their heaves at top basement level (Figure 6).
200 Heaves were measured in the displacement direction (i.e. parallel to the corrugations –
201 compare corrugations on Figure 4 with direction of heaves measurements on Figure 6a). The
202 block-bounding faults exhibiting both geometrical linkages (i.e. overlapping and merging of
203 the slip surfaces, Figure 6a) and complementary heaves are likely to have accommodated the
204 same episode of regional extension and so were likely active over the same time interval
205 (Cartwright et al., 1995; Cowie et al., 2005) as observed from the distribution of extension
206 over multiple faults during the progressive strain localization in the Corinth Rift system
207 (Nixon et al., 2016). Three main sets of faults (Figure 6) can be identified within the 3D
208 volume, each outlined on the depth and amplitude maps of S (coloured solid lines on Figure
209 4) by narrow distortions in the topography of S, changes in the orientations of the
210 corrugations on S and related change in the orientation of the strike of the faults remaining
211 approximately orthogonal to the corrugations. The easternmost set (closest to Iberia) consists
212 of four directly linked main faults (F3.0, F3.1, F3.2 and F4.0 on Figures 6a). The blocks
213 between F4.0 and F3.0 and between F3.0 and F3.1 pinch out southwards and northwards
214 respectively: these faults probably developed separately but became geometrically linked
215 when increasing displacement led to merger (Gupta and Scholz, 2000; Cowie et al., 2005) and
216 to form a single slip surface (Figure 6a, b). Within the entire fault set 3/4, as the heave on one
217 fault decreases, it increases elsewhere, but the sum of the heaves remains steady, even though
218 it decreases slightly to the north (Figure 6c), consistent with a general northward propagation
219 of rifting (Whitmarsh and Miles, 1995).

220 The geometrical linkages between the fault planes F3.0, F3.1, F3.2 and F4.0 (Figure 6a), and
221 the complementarity of the heaves within fault set 3/4 (Figure 6c), suggest that at times
222 during their evolution, F3.0, F3.1, F3.2 and F4.0 were active concurrently (Figure 6b), not
223 sequentially as previously suggested on the basis of 2D data (F3.0 then F4.0 - Ranero and
224 Pérez-Gussinyé, 2010). Although the 3D data require that Fault 3.1 was active over the same
225 time intervals as both Fault 3.0 and Fault 4.0, when looking at the fault system in 2D it might
226 be considered that F3.0 died abruptly when F4.0 initiated so that F3.0 and F4.0 were never
227 active at the same time, as in a 2D sequential faulting mechanism where a fault must lock-up
228 before the next fault forms (Ranero and Pérez-Gussinyé, 2010). However, it is generally
229 accepted that faults initiate as laterally restricted structures which grow both in length and in
230 displacement (Figure 6b) through repeated slip events (e.g. Cartwright et al., 1995; Cowie et
231 al., 2005; Nixon et al., 2016), making it unlikely that when F3.0 ceased to slip F4.0 was
232 instantly of sufficient extent to take up all the divergence accommodated further south by
233 F3.1. The 3D nature of rift fault network development thus far more likely implies that
234 activity on F4.0 and F3.0 overlapped in time (Figure 6b), probably substantially, as the
235 accommodation of the extension was progressively transferred from F3.0 to F4.0 as the locus
236 of extension migrated gradually oceanward. In short, the way faults grow, their linkages and
237 limited lateral extent, and the 3D nature of extension require modification of the 2D rolling
238 hinge model (Buck, 1988) as multiple faults have slipped at once (Figure 6b), and not in the
239 sequential way as defined by Ranero and Pérez-Gussinyé (2010) where two faults can not be
240 active at the same time, even if late extension migrated oceanwards. We note that overlap in
241 the activity of individual faults seems to be a common feature observed in natural 3D fault
242 systems even where faulting migrates asymmetrically (Colletini et al., 2009; Nixon et al.,
243 2016).

244 The observed geometrical linkages, slip surface merging and heave complementarity within
245 fault set 3/4 is thus a direct consequence of the 3D nature of extension, which also applies to
246 other fault sets identified within the 3D volume. Oceanward, F5.1 marks the start of fault set 5
247 (Figure 6d) as F5.1 cuts slightly across the S reflector to the east but is continuous with S to
248 the west (Figure 5a). Faults within set 5 (F5.1, 5.2, 5.3, 5.4) in places merge directly (see F5.3
249 and 5.4 on Figures 4 and 5a), and have complementary heaves (Figure 6d), so again are likely
250 to have been active concurrently. Stepping oceanward once more, within fault set 6 (Figure
251 6e; F6.0, F6.1, F6.4, trending more NNE-SSW), the heaves of the faults are complementary
252 again (Figure 6e), as one fault dies out its displacement is transferred to neighbouring faults
253 (Walsh et al., 2003; Fossen and Rotevatn, 2016) and the sum of the heaves remains
254 approximately constant across the volume.

255 In each fault set, the most landward fault, marking the eastern boundary of the set, (e.g. F5.1,
256 F6.4) appears to cut across the S reflector to the east and to be continuous with S to the west
257 (Figures 3, 5a and 5b), consistent with a rolling hinge model in which each new fault set
258 propagates up from the root zone at an angle to the preceding, more landward fault set. This
259 relationship both indicates that the faulting migrated oceanwards, as in the sequential faulting
260 model (Ranero and Pérez-Gussinyé, 2010), as each set cut across those landwards, and
261 precludes the possibility that all faults were active at the same time (Hoffmann and Reston,
262 1992). Conversely, the lack of any distortion of S where intersected by other faults within
263 each set confirms that these faults were active over the same time interval so that S was active
264 beneath the faults within that set, removing any topography on S. Thus, we interpret the
265 margin evolution in terms of a 3D rolling hinge model, with faulting migrating oceanwards,
266 with the limited lateral extent of individual faults requiring that several faults were active over
267 the same time interval. We conclude our analysis by focusing on the mechanics and timing of
268 the development of this three-dimensional rolling hinge system.

269 3.3 Timing and angle of slip on S

270 On the 2D data, the internal stratigraphy of the fault blocks is not well resolved, leaving
271 considerable uncertainty in the angle at which S slipped (Reston et al., 2007). The improved
272 spatial resolution provided by the 3D volume (Supplementary Figure S1) reveals the internal
273 structure of the fault blocks, showing that S developed late in the rifting evolution and slipped
274 at low-angle (Figure 7). Crystalline basement, sampled by submersible (Boillot et al., 1988)
275 and identified more widely from seismic velocities (Bayrakci et al., 2016; Davy et al., 2018),
276 is overlain by a thin internally poorly reflective package (*A*), that we interpret as predating the
277 current fault blocks (Figures 5 and 7). Overlying *A* is a thicker, more ubiquitous and reflective
278 series of sediments (*B*); small offsets in the fine layering of package *B* show that this unit is
279 intensely fractured and faulted. Near the bounding faults, *B* exhibits an internally poorly
280 reflective facies (Figures 7a and 7b), which thins markedly away from the fault scarps, to
281 grade laterally into a reflective, layered facies subparallel to the tops of the fault blocks. The
282 changing facies may be interpreted as wedge-shaped, internally chaotic debris flows resulting
283 from mass-wasting of the emerging fault scarps during seismogenic slip, which grade away
284 from the fault scarps into more layered turbidites (Boillot and Winterer, 1988; Boillot et al.,
285 1988) deposited within and along the half-grabens between adjacent block crests. Each
286 occurrence of package *B* is thus consistent with deposition during slip on the fault
287 immediately landward; where fault activity was diachronous, then so would be the deposition
288 of package *B*. The uppermost, and hence youngest, package (*C*) beneath the postrift (Figures
289 5 and 7) in places neither shows syn-tectonic fanning, nor always reaches the fault scarp.
290 Instead, it onlaps the upper portion of *B* and is thus interpreted as synrift, but post-dating local
291 faulting.

292

293 Within syn-faulting package *B*, the more continuously layered beds away from the fault are
294 likely to have been deposited close to horizontal and then rotated during slip on the block-
295 bounding faults. Consequently, the angular relationships between the faults and both the base
296 and the top of this part of package *B* (Figure 7), revealed by the depth conversion, can be used
297 to infer that the faults formed at 55-60°, were rotated to ca. 40° and then abandoned,
298 consistent with standard models of extensional faulting (Anderson, 1905; Sibson, 1985).
299 From the angle between package *B* (base and top) and the underlying *S* detachment, the faults
300 initially rooted at ca. 40° but, rotating as the block rotated, the downward continuation of each
301 fault at the level of top mantle (i.e. *S*) remained active until 20-25° (the angle measured
302 between the top of package *B* and *S* – Figure 7). Then a new fault propagated up at ~60° from
303 where *S* dipped at 40° and the process repeated.

304

305 The consistency of the angular relationships between sedimentary package *B*, *S* detachment,
306 and the faults within each half-grabens across the volume (Figures 5 and 7) supports the idea
307 that all blocks have been through the same process, as expected for a rolling hinge (Buck,
308 1988; Choi et al., 2013) rooting beneath the conjugate margin (Hopper et al., 2004; Reston
309 and McDermott, 2011) or a similar sequential faulting system (Ranero and Pérez-Gussinyé,
310 2010). However, the angular relationships measured from the 3D volume imply that this
311 system allowed slip on *S* at angles as low as 20-25°. Slip at such a low angle requires very
312 weak fault rocks such as talc or serpentine (Moore et al., 1996; Escartin et al., 1997; Pérez-
313 Gussinyé and Reston, 2001; Reston et al., 2007), high fluid pressures (Floyd et al., 2001) that
314 are difficult to maintain in an extensional environment (Wills and Buck, 1997), or both
315 (Reston et al., 2007). At extensional detachments formed at the base of the crust during Neo-
316 Tethyan rifting and exposed in the Alps, the fault rocks consist of serpentine gouge (Picazo et
317 al., 2013) and foliated serpentinites (Manatschal et al., 2006); similar serpentine lithologies

318 have been drilled further west at the Iberian margin (Whitmarsh et al., 1998) and inferred
319 from the reduction in mantle velocity beneath S (Bayrakci et al., 2016), but S itself has not
320 been sampled and other hydrated mantle rocks and even transient high fluid pressures may
321 also be important. Whatever the precise cause of fault weakening at the top of the mantle, the
322 large volumes of water needed (Bayrakci et al., 2016) require that the crust had thinned
323 sufficiently (~10 km) to become entirely brittle (Pérez-Gussinyé and Reston, 2001; Reston
324 and Pérez-Gussinyé, 2007) and so allow the necessary ingress of water (Bayrakci et al., 2016)
325 from above, penetrating several km into the brittle mantle. Subsequent slip and deformation
326 would then result in further water influx and further mantle hydration beneath the thinning
327 crust (Bayrakci et al., 2016; Prada et al., 2017). The development of a late stage asymmetric
328 detachment system during the rifting is compatible with the widely observed asymmetry at
329 conjugate magma-poor margin pairs (Gerlings et al., 2012; Reston, 2010), which is only
330 developed when the crust is thinner than ~10 km (Reston and Pérez-Gussinyé, 2007; Reston,
331 2010), that is where it had become entirely brittle during rifting, allowing serpentinization.
332 The numerical models of Brune et al. (2014) also predicted the development of asymmetry
333 through sequential faulting when the crust was thinned to between 10 and 20 km, depending
334 on lithospheric rheology, but their mechanism relied on the presence of a weak lower crustal
335 channel where temperatures were between 600° and 800°C, incompatible with the inferred
336 presence of serpentinites or similar rocks that only form below ~ 400°C (Emmanuel and
337 Berkowitz, 2006).

338

339 **4 CONCLUSIONS**

340 The 3D observations provide new insights into the role of detachment faulting during breakup
341 (Figure 8). The data demonstrate that S was not a throughgoing detachment active
342 simultaneously over a wide area, but rather a detachment fault formed of the root zones of

343 successive normal faults, a result never demonstrated before. In addition, the intersection of
344 one fault by the next, hence more recent, fault generation along the S reflector prove that
345 extensional faulting migrated oceanwards, aspects similar to the sequential faulting (Ranero
346 and Pérez-Gussinyé, 2010) and rolling hinge (Buck, 1988) models.

347

348 There are, however, three fundamental differences from existing 2D rolling hinge and
349 sequential faulting models. First, each fault is of limited lateral extent, requiring several
350 linked faults to have been active concurrently rather than only one major fault active at any
351 time. Thus, in 3D (Figure 8), the detachment grows through the complex interaction of
352 several faults at any one time. Second, these faults rooted onto S, which continued to slip at
353 low-angle (although rooting more steeply), requiring the presence of weak hydrated rocks
354 such as serpentinites (Bayrakci et al., 2016) beneath the thin continental crust. Third, the need
355 for mantle hydration indicates that the asymmetric detachment system only developed late in
356 the rifting history as the crust became entirely brittle and thus thinned to <10 km (Reston and
357 Pérez-Gussinyé, 2007; Bayrakci et al., 2016). This result is consistent with the observed
358 asymmetry of conjugate magma poor margin pairs (Reston, 2010) and contrasts with previous
359 models in which sequential faulting and hence asymmetric rifting either developed when the
360 crust was either >20 km thick (Ranero and Pérez-Gussinyé, 2010), or was controlled by a hot,
361 ductile lower crust (Brune et al., 2014), incompatible with the observed mantle
362 serpentinization.

363

364 **5 ACKNOWLEDGMENTS**

365 Data acquisition was funded by the National Science Foundation (OCE-257 1031769) and
366 UK Natural Environment Research Council (NERC) awards NE/E015883/1 and
367 NE/E016502/1. TAM was supported by a Wolfson Research Merit award. Data processing by

368 Repsol was funded by NERC through grant NE/E015883/1. We thank the crew of *R/V*
369 *Marcus G. Langseth*. We are grateful to Nur Schuba for helpful discussion concerning figure
370 4b. Reviews were by Marta Pérez-Gussinyé and an anonymous but helpful reviewer.

371

372 6 REFERENCES

373 Anderson, E.M., 1905. The dynamics of faulting, *Trans. Edinburgh Geol. Soc.*, 8 (3), 387-
374 402.

375 Barker, P.F., and Burrell, J., 1977. The opening of Drake Passage. *Marine Geology*, 25, 15-
376 34, [https://doi.org/10.1016/0025-3227\(77\)90045-7](https://doi.org/10.1016/0025-3227(77)90045-7).

377 Bayrakci, G., Minshull, T.A., Sawyer, D.S., Reston, T.J., Klaeschen, D., Papenberg, C.,
378 Ranero, C., Bull, J.M., Davy, R.G., Shillington, D.J., Pérez-Gussinyé, M., Morgan, J.K.,
379 2016. Fault-controlled hydration of the upper mantle during continental rifting. *Nat.*
380 *Geosci.* 9, 384-388, DOI: 10.1038/NGEO2671.

381 Boillot, G., and Winterer, E. L., 1988. Drilling on the Galicia Margin: retrospect and prospect.
382 *Proc. ODP Sci. Results* 103, 809–828.

383 Boillot, G., Comas, M. C., Girardeau, J., Kornprobst, J., Loreau, J.-P., Malod, J., Mougénot,
384 D. & Moullade, M., 1988. Preliminary results of the Galinaute Cruise: Dives of the
385 submersible Nautille on the western Galicia margin. *Proc. ODP Sci. Results* 103, 37-51.

386 Brune, S., Heine, C., Pérez-Gussinyé, M., and Sobolev, S.V, 2014. Rift migration explains
387 continental margin asymmetry and crustal hyper-extension. *Nature Commun.* 5:4014,
388 DOI: 10.1038/ncomms5014.

389 Buck, W. R, 1988. Flexural rotation of normal faults. *Tectonics* 7, 959–973,
390 <https://doi.org/10.1029/TC007i005p00959>.

391 Bullard, E.C., Everett, J.E., Smith, A.G., 1965. The fit of the continents around the Atlantic.
392 Philosophical transactions of the Royal Society of London. Series A, Mathematical and
393 physical sciences, 258, 1088, 41-51.

394 Cann, J.R., Blackman, D.K., Smith, D.K., McAllister, E., Janssen, B., Mello, S., Avgerinos,
395 E., Pascoe, A.R., Escartin, J., 1997. Corrugated slip surfaces formed at North Atlantic
396 ridge-transform intersections. *Nature* 385, 329–332.

397 Cartwright, J. A., Trudgill, B. D., Mansfield, C. S., 1995. Fault growth by segment linkage:
398 an explanation for scatter in maximum displacement and trace length data from the
399 Canyonlands Grabens of SE Utah. *J. Struct. Geol.* 17, 1319 -1326,
400 [https://doi.org/10.1016/0191-8141\(95\)00033-A](https://doi.org/10.1016/0191-8141(95)00033-A).

401 de Charpal, O., Guennoc, P., Montadert, L. & Roberts, D.G., 1978. Rifting, crustal
402 attenuation and subsidence in the Bay of Biscay. *Nature* 275, 706–711.

403 Choi. E., Buck, W.R., Lavier, L.C., Petersen, K.D., 2013. Using core complex geometry to
404 constrain fault strength. *Geophysical Research Letters*, VOL. 40, 3863–3867,
405 doi:10.1002/grl.50732, 2013.

406 Collettini, C., Viti, C., Smith, S.A.F., and Holdsworth, R.E., 2009. Development of
407 interconnected talc networks and weakening of continental low-angle normal faults.
408 *Geology*, June 2009, v. 37; no. 6; p. 567–570; doi: 10.1130/G25645A.1;

409 Cowie, P.A., Underhill, J.R., Behn, M.D., Lin, J., and Gill, C.E., 2005. Spatio-temporal
410 evolution of strain accumulation derived from multi-scale observations of Late Jurassic
411 rifting in the northern North Sea: a critical test of models for lithospheric extension.
412 *Earth Planet. Sci. Lett.* 234, 401–419, doi:10.1016/j.epsl.2005.01.039.

413 Davy, R.G., Morgan, J.V., Minshull, T.A., Bayrakci, G., Bull, J.M., Klaeschen, D., Reston,
414 T.J., Sawyer, D.S., Lymer, G., Cresswell, D., 2018. Resolving the fine-scale velocity
415 structure of continental hyperextension at the Depp Galicia Margin using full-waveform

416 inversion. *Geophysical Journal International*, 212, Issue 1, Pages 244–
417 263, <https://doi.org/10.1093/gji/ggx415>.

418 Edwards, J.H., Kluesner, J.W., Silver, E.A., Brodsky, E.E., Brothers, D.S., Bangs, N.L.,
419 Kirkpatrick, J.D., Wood, R., Okamoto, K., 2018. Corrugated megathrust revealed
420 offshore from Costa Rica, *Nature Geoscience*, 11, pages 197–202, (2018),
421 doi:10.1038/s41561-018-0061-4.

422 Emmanuel, S. and Berkowitz, B., 2006. Suppression and stimulation of seafloor
423 hydrothermal convection by exothermic mineral hydration. *Earth Planet. Sci. Letts.* 243,
424 6567-668.

425 Escartin, J., Hirth, G., and Evans, B., 1997. Effects of serpentinization on the lithospheric
426 strength and the style of normal faulting at slow-spreading ridge. *Earth Planet. Sci. Letts.*
427 151, 181-189, [https://doi.org/10.1016/S0012-821X\(97\)81847-X](https://doi.org/10.1016/S0012-821X(97)81847-X).

428 Floyd, J. S., Mutter, J. C., Goodliffe, A. M., and Taylor, B., 2001. Evidence for fault
429 weakness and fluid flow within an active low-angle normal fault. *Nature* 411, 779–783.

430 Fortey, R.A., and Cocks, L.R.M., 2003. Palaeontological evidence bearing on global
431 Ordovician–Silurian continental reconstructions. *Earth-Science Reviews*, 61, 245–307,
432 [https://doi.org/10.1016/S0012-8252\(02\)00115-0](https://doi.org/10.1016/S0012-8252(02)00115-0).

433 Fossen, H., and Rotevatn, A., 2016. Fault linkage and relay structures in extensional settings –
434 A review. *Earth Science Reviews*, 154, 14-28,
435 <https://doi.org/10.1016/j.earscirev.2015.11.014>

436 Gerlings, J., Loudon, K.E., Minshull, T.A., and Nedimovic, M.R., 2012. Flemish Cap-Goban
437 Spur conjugate margins: New evidence of asymmetry. *Geology*; 40;1107-1110,
438 <https://doi.org/10.1130/G33263.1>.

439 Goldsworthy, M., and Jackson, J., 2001. Migration of activity within normal fault systems:
440 examples from the Quaternary of mainland Greece. *Journal of Structural Geology* 23,
441 489-506, [https://doi.org/10.1016/S0191-8141\(00\)00121-8](https://doi.org/10.1016/S0191-8141(00)00121-8).

442 Gupta, A., and Scholz, C. H., 2000. A model of normal fault interaction based on
443 observations and theory, *J. Struct. Geol.* 22, 865-879, [https://doi.org/10.1016/S0191-](https://doi.org/10.1016/S0191-8141(00)00011-0)
444 [8141\(00\)00011-0](https://doi.org/10.1016/S0191-8141(00)00011-0).

445 Hoffmann, H-J., and Reston, T.J., 1992. The nature of the S reflector beneath the Galicia
446 Banks rifted margin: Preliminary results from pre-stack depth migration, *Geology*, 20,
447 1091-1094, doi:10.1130/0091-7613.

448 Hopper, J., Funck, T., Tucholke, B.E., Larsen, H.C., Holbrook, W.S., Loudon,
449 K.E., Shillington, D. and Lau, H., 2004. Continental breakup and the onset of ultraslow
450 seafloor spreading off Flemish Cap on the Newfoundland rifted margin. *Geology* 32, 93-
451 96, <https://doi.org/10.1130/G19694.1>.

452 Huismans, R.S., and Beaumont, C., 2003. Symmetric and asymmetric lithospheric extension:
453 relative effects of frictional-plastic and viscous strain softening. *Journal of Geophysical*
454 *Research*, 108, NO. B10, 2496, <https://doi.org/10.1029/2002JB002026>.

455 Le Pichon, X., and Sibuet, J.-C., 1981. Passive margins: A model of formation. *Journal of*
456 *Geophysical Research*, 86(B5): 3708–3720.doi:10.1029/JB086iB05p03708.

457 Lentini, M.R., Fraser, S.I., Sumner, H.S., Davies, R.J., 2010. Geodynamics of the central
458 South Atlantic conjugate margins: implications for hydrocarbon potential. *Petroleum*
459 *Geoscience*, Vol. 16, 2010, pp. 217–229, DOI 10.1144/1354-079309-909

460 Leythaeuser, T., Reston, TJ, and Minshull, TA, 2005. Waveform inversion of the S reflector
461 west of Spain: Fine structure of a detachment fault. *Geophys Res. Letts.*, 32, L22304,
462 doi:10.1029/2005GL024026.

463 Lister, G.S., Etheridge, M.A., Symonds, P.A., 1986. Detachment faulting and the evolution of
464 passive continental margins. *Geology*, v 14, 246-250, [https://doi.org/10.1130/0091-](https://doi.org/10.1130/0091-7613(1986)14<246:DFATEO>2.0.CO;2)
465 [7613\(1986\)14<246:DFATEO>2.0.CO;2](https://doi.org/10.1130/0091-7613(1986)14<246:DFATEO>2.0.CO;2).

466 Manatschal, G., Engstrom, A., Desmurs, L., Schaltegger, U., Cosca, M., Muentener, O.,
467 Bernoulli, D., 2006. What is the tectono-metamorphic evolution of continental break-up:
468 The example of the Tasma Ocean-Continent Transition. *J. Struct Geology*, 28, 1849-
469 1869, DOI: [10.1016/j.jsg.2006.07.014](https://doi.org/10.1016/j.jsg.2006.07.014).

470 Moore, D.E., Lockner, D.A., Summers, R., Shengli, M. and Byerlee, J.D., 1996. Strength of
471 chrysotile-serpentinite gouge under hydrothermal conditions: Can it explain a weak San
472 Andreas fault? *Geology*, 24, 1041–1044.

473 Nixon, C. W., McNeill, L., Bull, J., Bell, R., Gawthorpe, R., Henstock, T., Christodoulou, D.,
474 Ford, M., Taylor, B., Sakellariou, D., Ferentinos, G., Papatheodorou, G., Leeder, M.R.,
475 Collier, R.E.LI., Goodliffe, A.M., Sachpazi, M., Kranis, H., 2016. Rapid spatiotemporal
476 variations in rift structure during development of the Corinth Rift, central Greece,
477 *Tectonics*, 35, 1225–1248, doi:10.1002/2015TC004026.

478 Pérez-Gussinyé, M., and Reston, T.J., 2001. Rheological evolution during extension at
479 nonvolcanic rifted margins: Onset of serpentinization and development of detachments
480 leading to continental breakup. *Journal of Geophysical Research*, 106, B3, 3961-3975,
481 <https://doi.org/10.1029/2000JB900325>.

482 Picazo, S., Manatschal, G., Cannat, M., Andreani, M., 2013. Deformation associated to
483 exhumation of serpentinized mantle rocks in a fossil Ocean Continent Transition: The
484 Totalp unit in SE Switzerland. *Lithos*, 175-176, 255-271,
485 <https://doi.org/10.1016/j.lithos.2013.05.010>.

486 Prada, M., Watremez, L., O'Reilly, B., Minshull, T.A., Chen, C., Reston, T.J., Shannon, P.,
487 Klaeschen, D., Wagner, G., Gaw, V., 2017. Crustal strain-dependent serpentinisation in

488 the Porcupine Basin, offshore Ireland. *Earth and Planetary Science Letters*, 474, 148-159,
489 <https://doi.org/10.1016/j.epsl.2017.06.040>.

490 Ranero, C.R., Pérez-Gussinyé, M., 2010. Sequential faulting explains the asymmetry and
491 extension discrepancy of conjugate margins. *Nature* 468, 294-300.

492 Resor, P.G., and Meer, V.E., 2009. Slip heterogeneity on a corrugated fault. *Earth Planet. Sci.*
493 *Letts.* 288, 483-491, <https://doi.org/10.1016/j.epsl.2009.10.010>.

494 Reston, T.J., 2010. The opening of the central segment of the South Atlantic: symmetry and
495 the extension discrepancy. *Petroleum Geoscience*, 16, 199-206,
496 <https://doi.org/10.1144/1354-079309-907>.

497 Reston, T.J., and McDermott, K.G., 2011. Successive detachment faults and mantle unroofing
498 at magma-poor rifted margins. *Geology*, **39**, 1071–
499 1074, <http://dx.doi.org/10.1130/G32428>.

500 Reston, T.J., Pérez-Gussinyé, M., 2007. Lithospheric extension from rifting to conti-
501 nental breakup at magma-poor margins: rheology, serpentinisation and sym-metry. *Int. J. Earth*
502 *Sci.* 96 (6), 1033–1046. <https://doi.org/10.1007/s00531-006-0161-z>.

503 Reston, T. J., Leythaeuser, T., Booth-Rea, G., Sawyer, D., Klaeschen, D., Long, C., 2007.
504 Movement along a low-angle normal fault: The S reflector west of Spain. *Geochem.*
505 *Geophys. Geosyst.* 8, 6, Q06002, <https://doi.org/10.1029/2006GC001437>.

506 Schuba, N.C., Gray, G.G., Morgan, J.K., Sawyer, D.S., Shillington, D.J., Reston, T.J., Bull,
507 J.M., Jordan, B.E., 2018. A low-angle detachment fault revealed: three-dimensional
508 images of the S-reflector fault zone along the Galicia passive mar-gin. *Earth Planet. Sci.*
509 *Lett.* 492, 232–238. <https://doi.org/10.1016/j.epsl.2018.04.012>.

510 Sibson, R.H., 1985. A note on fault reactivation. *J. Structural Geology*, 7, 751-754,
511 [https://doi.org/10.1016/0191-8141\(85\)90150-6](https://doi.org/10.1016/0191-8141(85)90150-6).

512 Sibuet, J. C, 1992. New constraints on the formation of the non-volcanic continental Galicia–
513 Flemish Cap conjugate margins. *J. Geol. Soc. Lond.* 149, 829–840,
514 <https://doi.org/10.1144/gsjgs.149.5.0829>.

515 Walsh, J.J., Bailey, W.R., Childs, C., Nicol, A., Bonson, C.G., 2003. Formation of segmented
516 normal faults: a 3-D perspective. *Journal of Structural Geology*, 25, 1251-1262,
517 doi:10.1016/j.jsg.2010.06.018.

518 Whitmarsh, R.B., Beslier, M.-O., Wallace, P.J., et al., 1998. Proceedings ODP, Initial
519 Reports, 173. Ocean Drilling Program, College Station, TX
520 <http://dx.doi.org/10.2973/odp.proc.ir.173.1998>.

521 Whitmarsh, R. B., and Miles, P. R., 1995. Models of the development of the West Iberia
522 rifted continental margin at 40°30'N deduced from surface and deep-tow magnetic
523 anomalies. *Journal of Geophysical Research*, 100, 3789–3806,
524 <https://doi.org/10.1029/94JB02877>.

525 Wills, S., and Buck, W.R., 1997. Stress-field rotation and rooted detachment faults: A
526 Coulomb failure analysis, *J. Geophys. Res.*, 102, 20, 503–20,514,
527 <https://doi.org/10.1029/97JB01512>.

528 7 FIGURES CAPTIONS

529 **Figure 1.** Detachment models. a) 2D model in which detachment slips at low-angle, multiple
530 faults active at once (Sibuet, 1992). b) 2D rolling hinge: detachment comprises the roots of
531 successive faults, active sequentially when steep (Reston et al., 2007; Bayrakci et al., 2016).
532 Faults are sequentially numbered in the chronological order from the oldest (Fault 1) to the
533 most recent and active one (Fault 4).

534 **Figure 2:** Location of the Galicia 3D volume west of Spain across the deep Galicia margin.
535 White box shows the location of the 3D reflection survey. Black dots show the location of
536 sites drilled during ODP leg 103. Isocontours show the bathymetry of the study area (in m).

537 Inset map from Google Earth. Bathymetric data consist in Global Multi-Resolution
538 Topography Data Synthesis from the National Oceanic and Atmospheric Administration.

539 **Figure 3.** The anatomy of the Galicia margin summarising the key structural and stratigraphic
540 elements. The figure displays a perspective view from the north of the 3D volume and has
541 been built by removing the post-rift sequence to expose the top of the faulted layer in the
542 southern part of the volume; similarly, the pre- and syn-rift sequences have been removed to
543 expose the top of the basement and the planes of the block-bounding fault in the northern part
544 of the volume. Two vertical slices generated through the northern and southern parts of the
545 volume respectively display the extended continental basement and the geometry of the pre-
546 and syn-rift units (A, B, C). The top of the faulted layer surface, the top basement surface and
547 the vertical slices reveal the lateral discontinuity and interactions of faults above S.
548 Corrugations on S surface (shown at the NW corner of the volume) match the corrugations
549 observed on the plane of the block-bounding faults propagating up from S (Fault 6.0). The
550 seismic data are shown with no vertical exaggeration.

551 **Figure 4.** Maps of the S reflector. a: Time map displaying corrugations, oblique to the sail-
552 lines and shown by three sets of coloured arrows corresponding to the three sets of block-
553 bounding faults rooting on S (solid lines). The long wavelength undulation of S in time is due
554 to velocity pull-up effects. Green dotted line underlines where S meets the crust-mantle
555 boundary b: Time filtered map obtained by subtracting the rough interpreted surface of S from
556 the smoothed surface of S in time. The corrugations (arrowed) are highlighted by ~10 ms
557 lineations. Traces of the deep segments of the block bounding faults on S (solid lines) are
558 highlighted by ~20 ms lineations. c: Depth map showing corrugations (arrowed) remaining
559 approximately orthogonal to the corresponding fault set and distortions of S where main
560 block-bounding faults (solid lines) root. S also shows a pronounced distortion where it meets
561 the crust-mantle boundary (green dotted line). d: Amplitude map of S, made by slicing

562 through the 3D volume along the peak of the envelope function. The corrugations visible in
563 depth appear as pronounced lineations of high amplitude.

564 **Figure 5.** Seismic reflection images from the Galicia 3D volume. a, c: Vertical time sections;
565 b, d: Same vertical sections converted to depth. The sections were generated through the 3D
566 volume in the same direction as the corrugations observed on S, thus oriented in the extension
567 and displacement direction (compare direction of sections on Figure 6 with corrugations on
568 Figure 4). The sections show a bright reflection (S) that meets the crust-mantle boundary
569 (white arrows) and runs at the base of the fault blocks. The mantle beneath S has been shown
570 by wide-angle velocities to be serpentized. S displays distortions where the block-bounding
571 faults root onto it, implying that S is composed of deep segments of faults. Long and short
572 horizontal arrows point the upward decrease in fault displacements (shown in km),
573 respectively between Top Basement and Top A, suggesting the faults propagated up from S.
574 E, f, g, h: Blow ups in time (e, g) and corresponding blow ups in depth (f, h) showing details
575 of relationship between S and overlying faults: F5.1 and F6.4 continue downdip as S, cutting
576 across an older segment of S. Horizontal bars show the heaves (see Figure 6) as, coloured by
577 fault set. Uninterpreted sections are shown in supplementary Figure S2 and details of the
578 analysis of the angle at which S slipped in Figure 7.

579 **Figure 6.** Heave analysis. a: Top basement map showing block-bounding faults heaves along
580 white flowlines (dashed when only partially covered by the data) defined by corrugations on
581 S; The white arrows point-out spatial linkage between different fault plans. Faults are
582 numbered after line IAM11 from Ranero and Pérez-Gussinyé (2010); b: Map view of fault
583 development in which several faults slip over the same period of time - designed for fault set
584 3/4 but also applicable to fault sets 5 and 6. New faults nucleate, grow and link in the rift-axis
585 area while former faults progressively deactivate, implying several active faults at different
586 stages of their evolution: nucleation, fully active, in process of deactivation and deactivated.

587 Arrows show the relative growth of the different faults. Looking at faults F3.0 and F4.0 on a
588 single 2D line (e.g. IAM11) only provides a glimpse of the full fault system and does not
589 allow to image faults lateral geometry, which form a single slip surface south of IAM11 when
590 merged with fault F3.1, as observed from the 3D data.

591 ; c: Cumulative and individual heaves with uncertainties for fault sets 3/4. Unless F4.0 is
592 included in set 3/4, the heaves drop off suddenly to the north at ~7km. Further north as the
593 heave on F4.0 gradually decreases, that on F3.0 gradually increases. Cumulative heave 3/4
594 decreases gradually to the north; all faults in this set were coeval; d: Cumulative and
595 individual heaves with uncertainties for fault set 5. Heave on fault F5.2 is transferred to F5.1,
596 then to F5.3; Cumulative heave 5 remains steady across the volume, all faults in this set were
597 coeval.; e: Cumulative and individual heaves with uncertainties for fault set 6. Moving north,
598 heave on F6.1 increases as that on F6.4 drops, and then transfers abruptly to F6.0; Cumulative
599 heave 6 remains steady across the volume, all faults in this set were coeval.; f: Cumulative
600 heave of all the faults across the dataset decreases slightly to the north.

601 **Figure 7:** Geometrical analysis of the angle at which faults and S were active based on flow
602 lines through the volume. See Figure 5 for location of data. a, c) current geometry shown in
603 Figure 5c. S dips at 3° to the west whereas the top and base of package B dip 17° and 34°
604 respectively to the east, implying that S dipped 37° W at the onset of deposition of package B
605 and 20° W when the top of package B was deposited horizontally. b, d) similar analysis for
606 the data in Figure 5d shows that S dipped 32° and 26° at the onset and end of deposition of
607 package B. e), f) geometry at the end of deposition of package B, not corrected for
608 compaction. g), h) geometry at the end of deposition of package B, corrected for compaction.
609 All show that S was active down to ~20° and that the faults were active down to ~40°.

610 **Figure 8:** Our summary model based on 3D observations. Extension migrates oceanwards,
611 but several faults (color-coded by set) were active simultaneously in each set, a 3D innovation

612 of the 2D model shown in figure 1b. The faults rooted on and propagated up from a
613 serpentine detachment (S) at the base of the crust; slip on S occurs at low-angles. The 3D
614 modified rolling hinge system developed only once the entire crust had thinned sufficiently to
615 become brittle allowing mantle hydration.

616

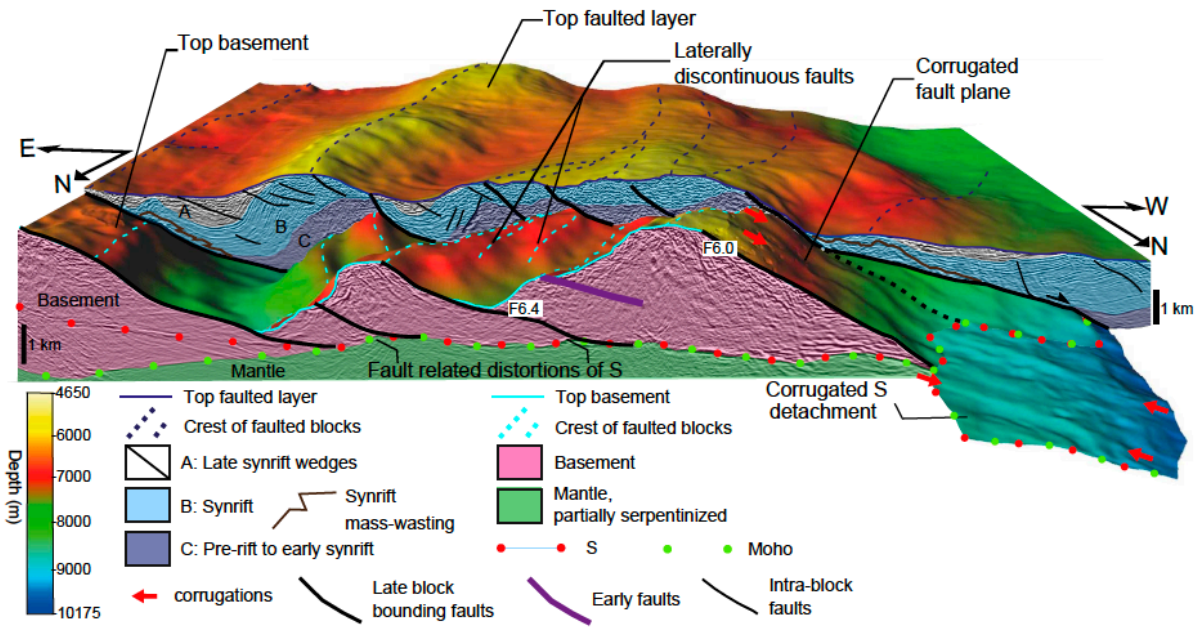
617 **Supplementary figures**

618 **Figure S1.** Comparison of 2D prestack depth migrated images with depth-converted versions
619 of 3D prestack time-migrated images. The close match verifies the accuracy of the depth
620 conversion and highlights the improved imaging resulting from 3D migration. (a) IAM11
621 prestack depth migrated image and faults numbering from Ranero and Pérez-Gussinyé (2010).
622 (b) corresponding section through the depth conversion of 3D prestack volume. Note also the
623 improved resolution of the sediments in the 3D volume and improved continuity of S.

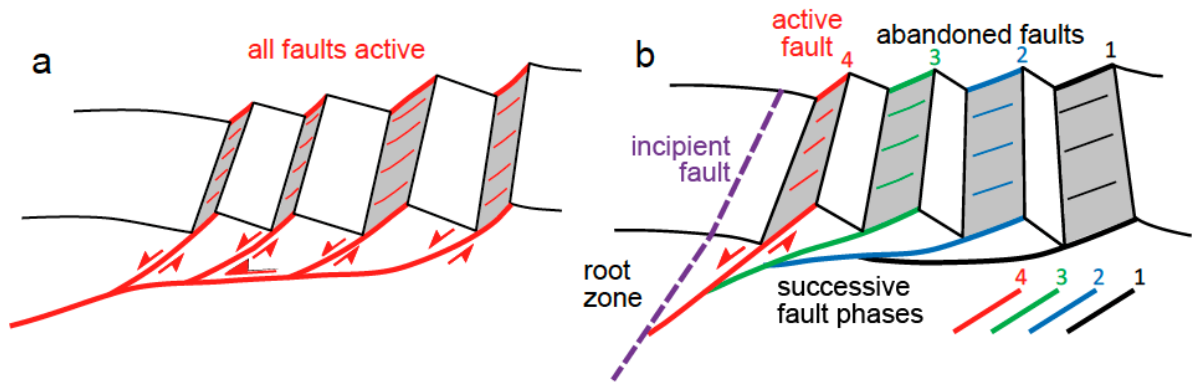
624 **Figure S2.** Uninterpreted versions of the data shown in Figure 5.

625 **Figure S3.** Uninterpreted versions of the data shown in Figure 4.

626



628 Graphical Abstract



629 Figure 1

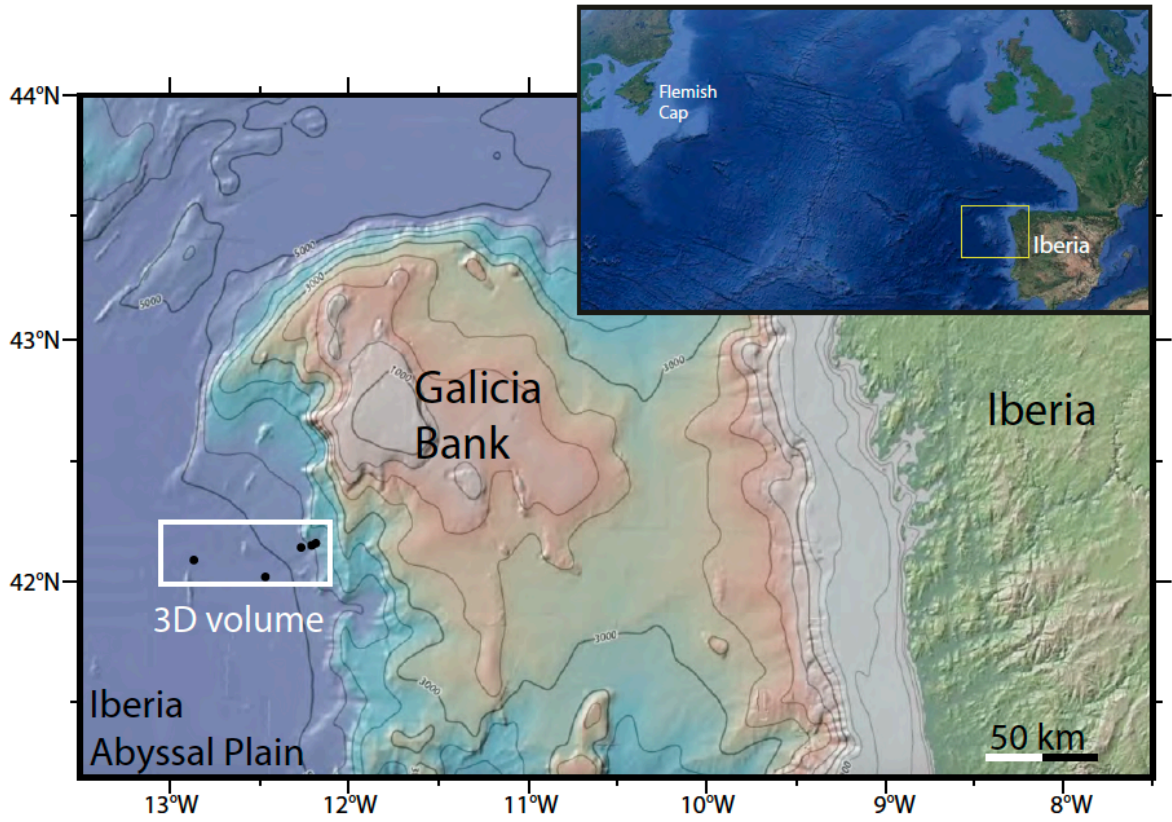


Figure 2

630

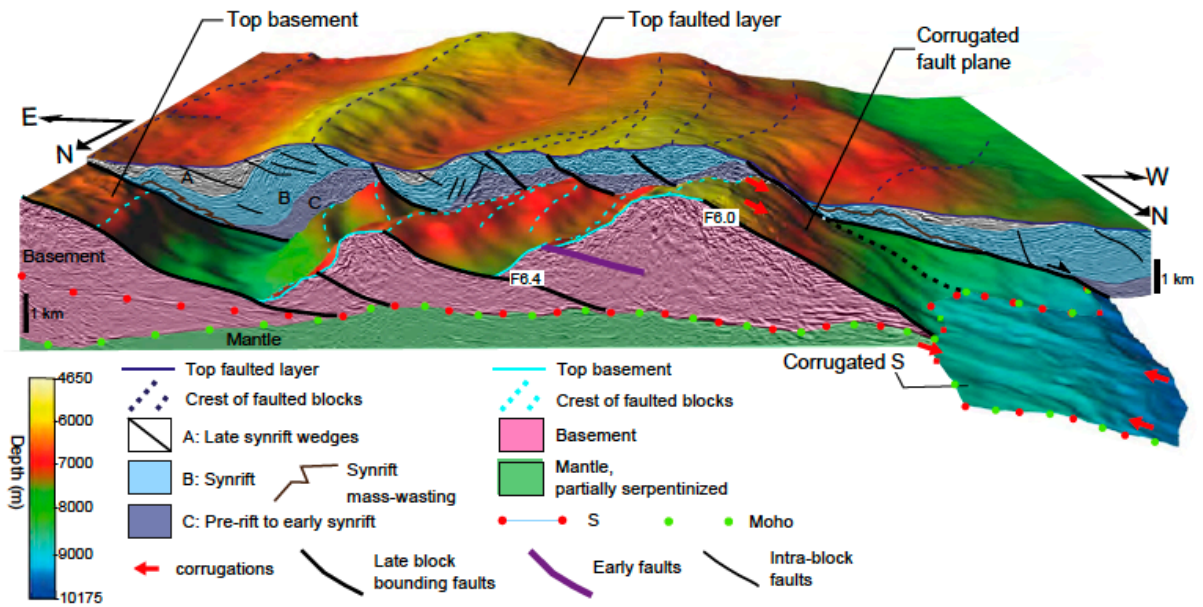


Figure 3

631

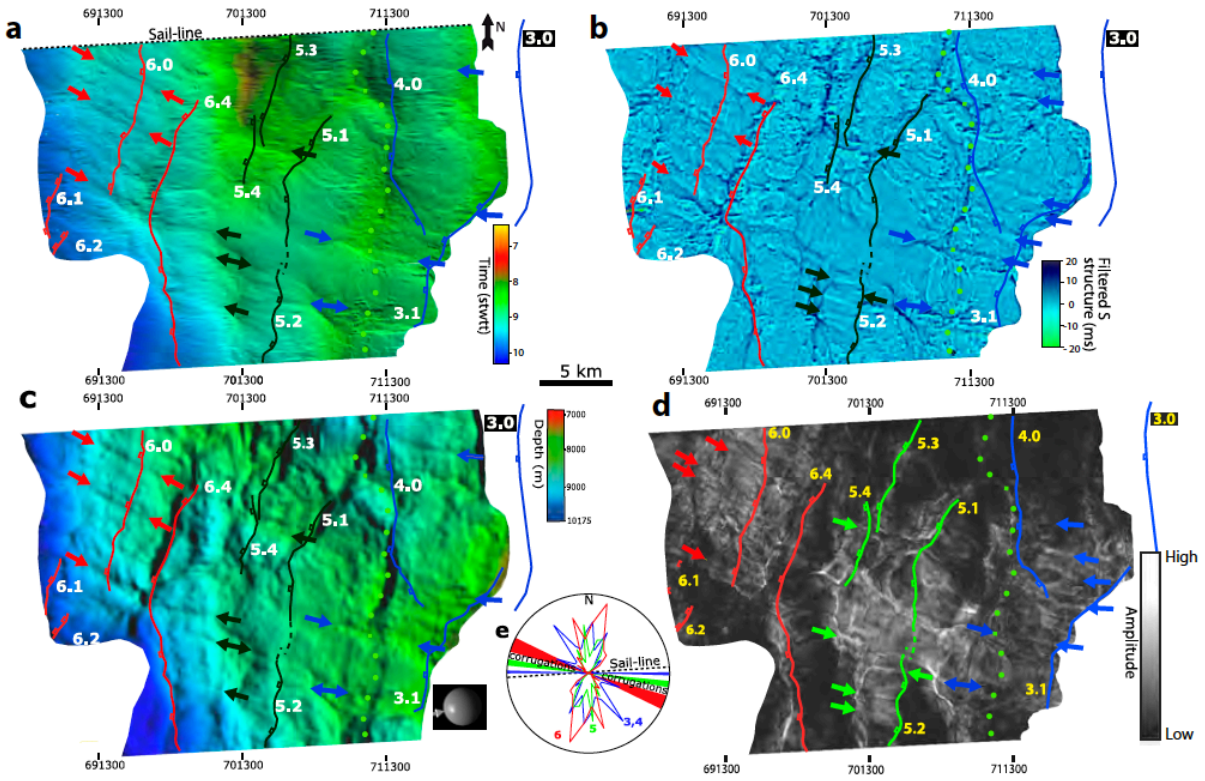


Figure 4

632

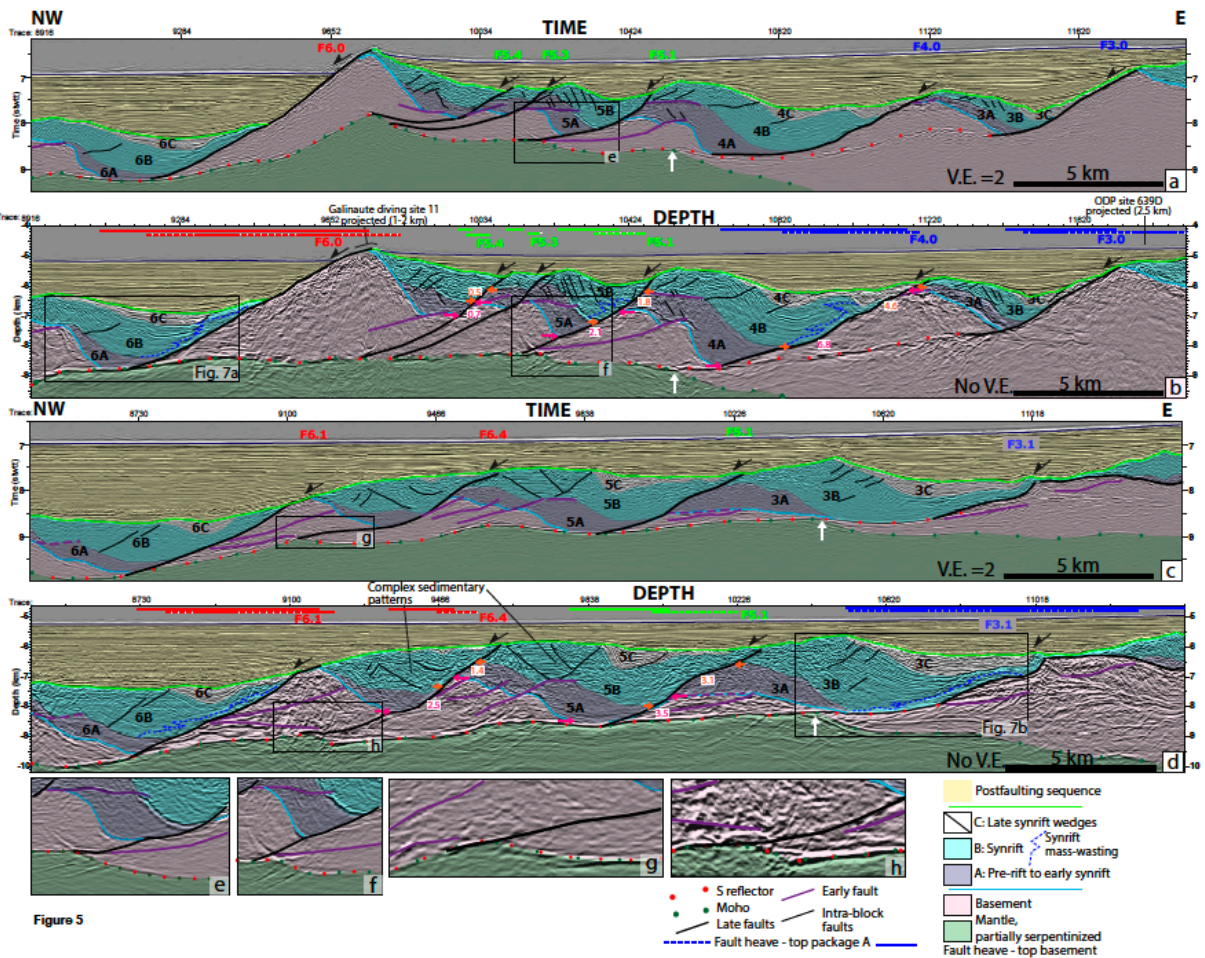
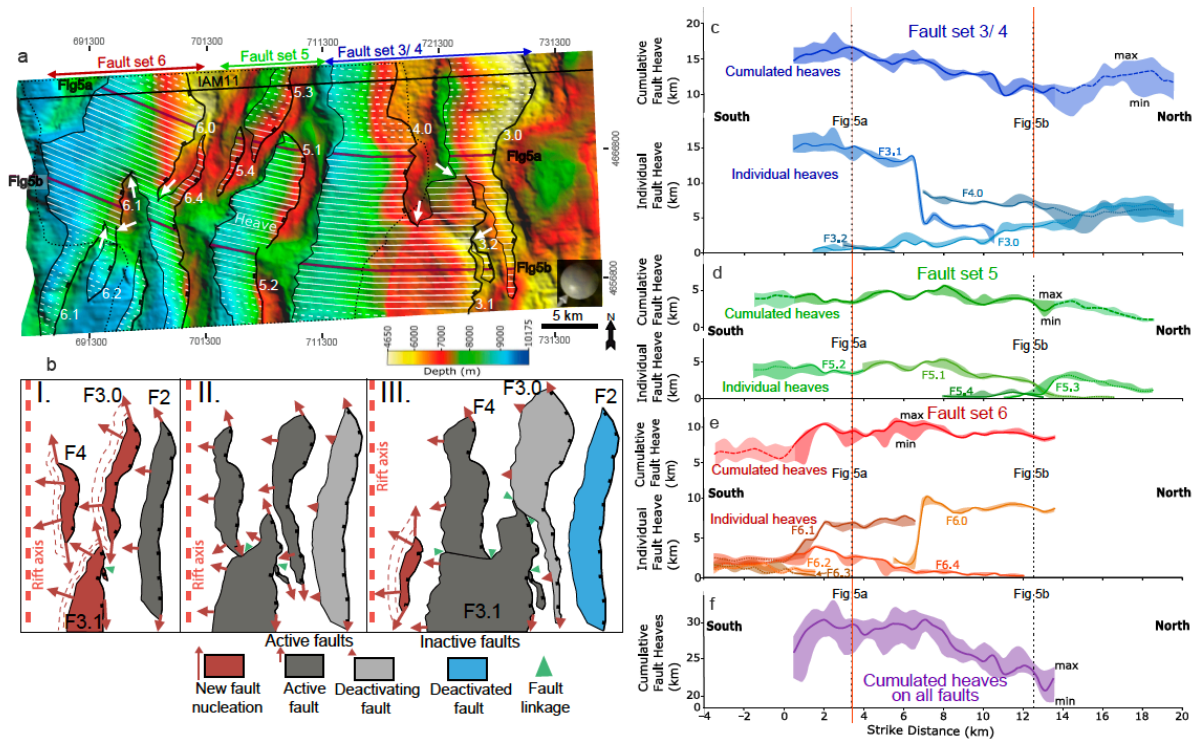


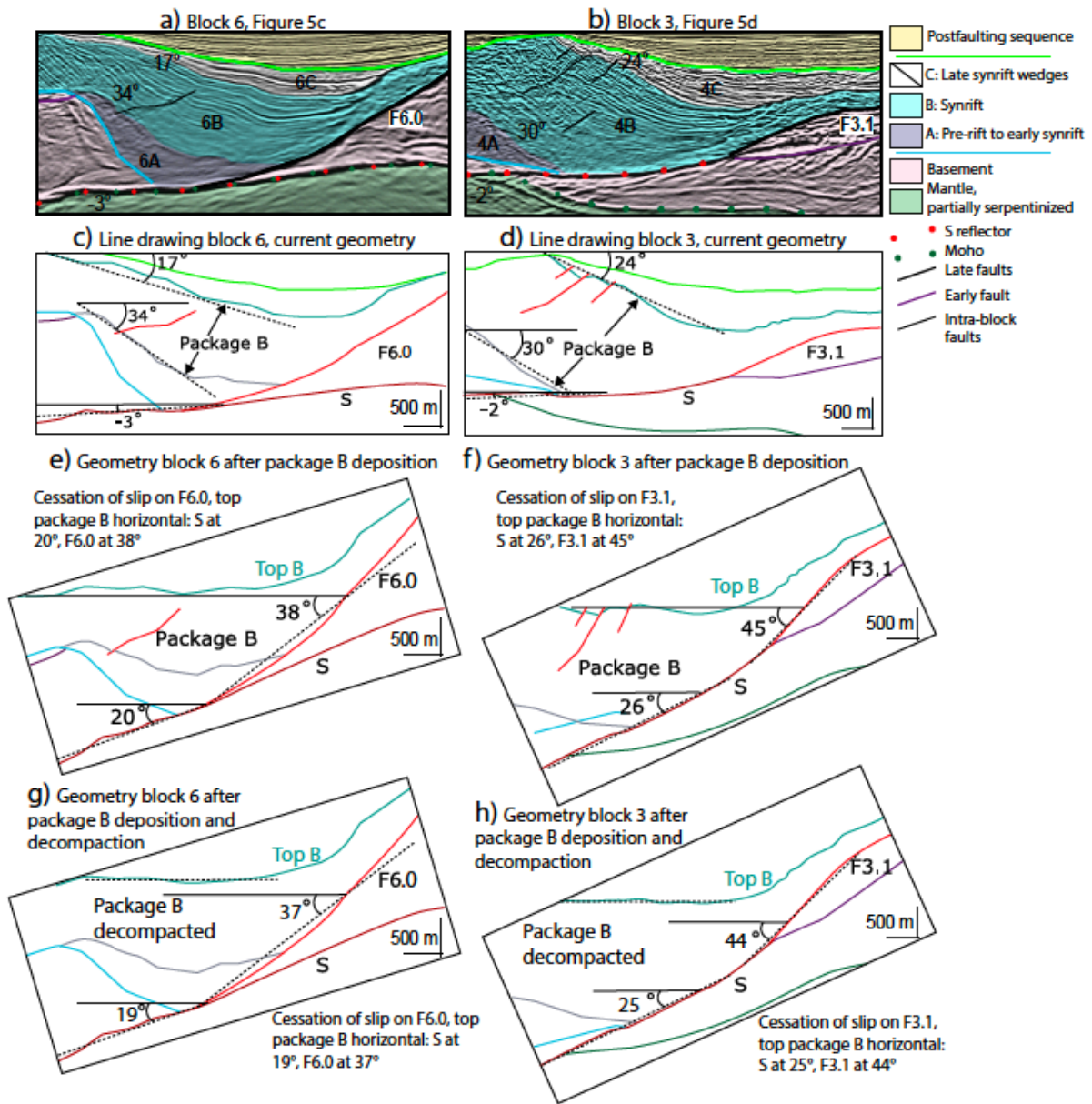
Figure 5

633



634

635 Figure 6



636

637 Figure 7

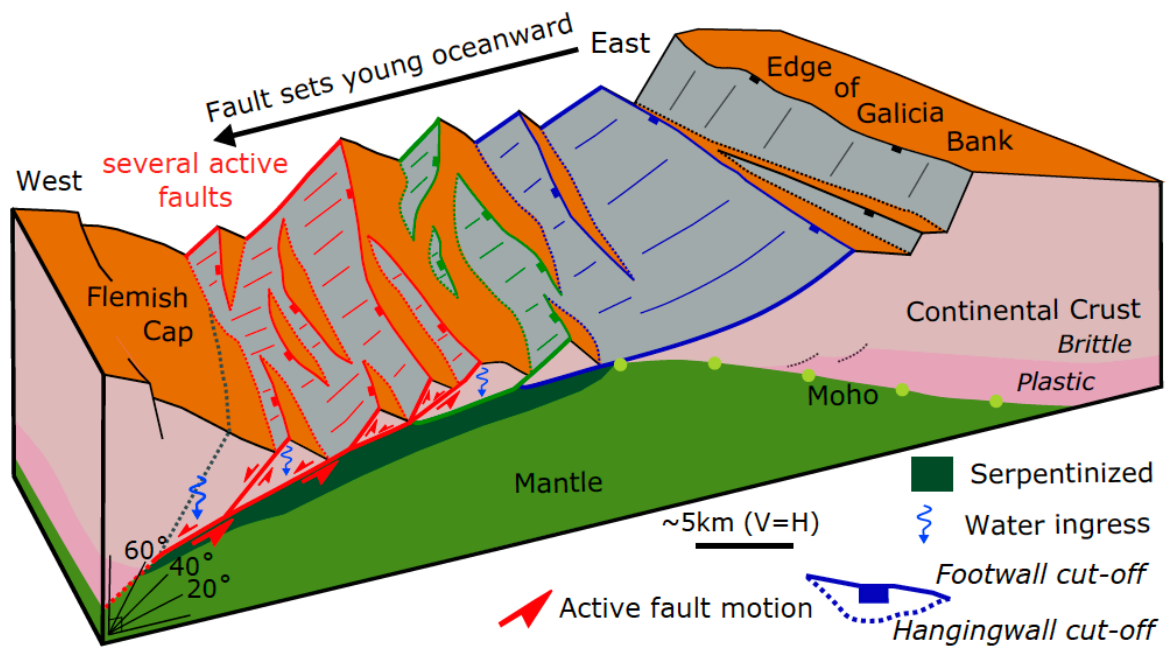
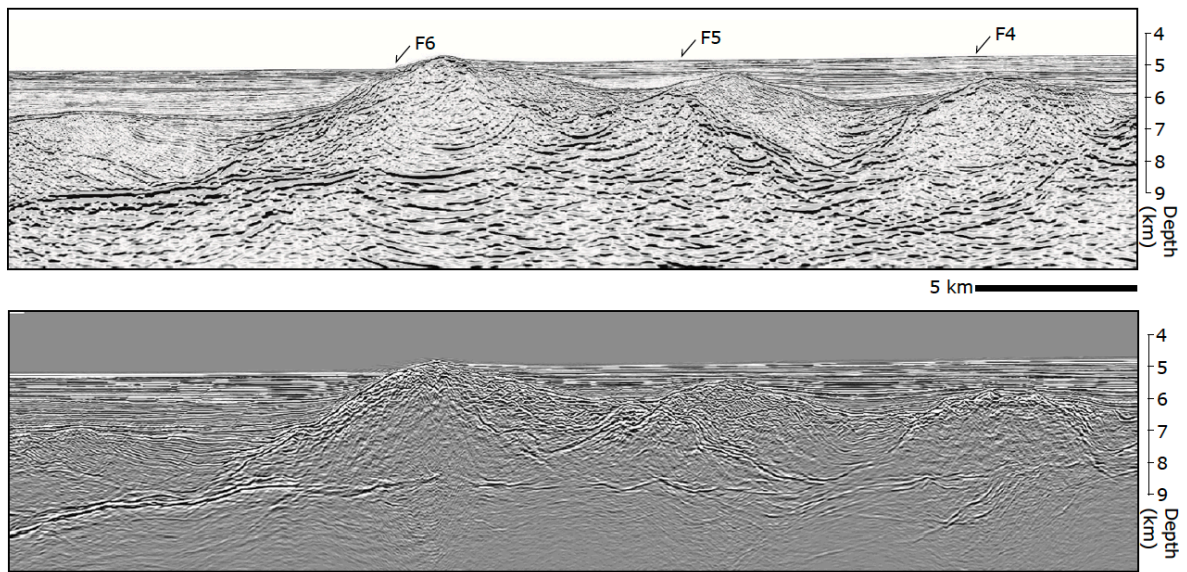


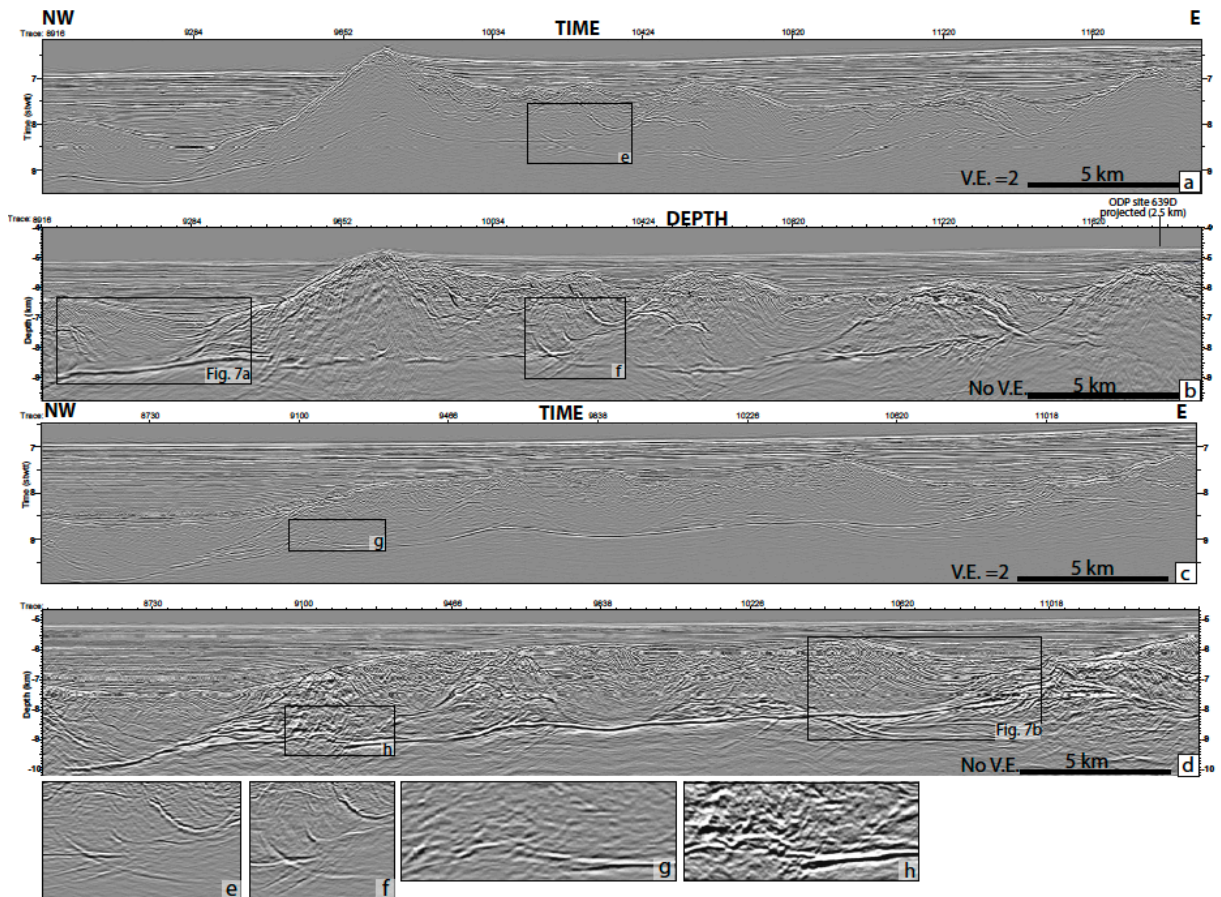
Figure 8

638



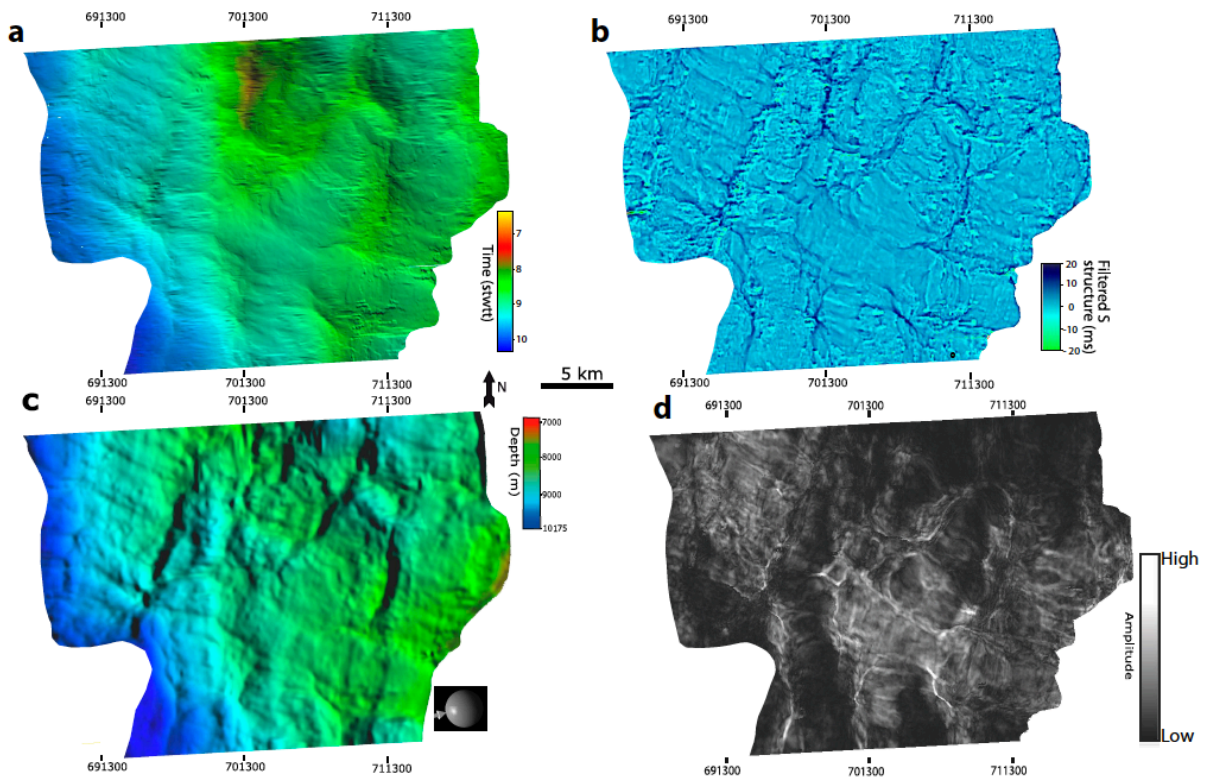
639

640 Supplementary Figure S1



641

642 Supplementary Figure S2



643

